J Mater Sci (2014) 49:4202–4214
DOI 10.1007/s10853-014-8115-5

Plastic deformation behavior of ultrafine-grained Al–Mg–Sc alloy

N. Kumar · M. Komarasamy · R. S. Mishra

Received: 7 November 2013 / Accepted: 14 February 2014 / Published online: 4 March 2014

Abstract Ultrafine-grained (UFG) Al–Mg–Sc alloy was obtained by friction stir processing. The UFG alloy was subjected to uniaxial tensile testing to study the tensile deformation behavior of the alloy. An inhomogeneous yielding (Lüdering phenomenon) was observed in the stress–strain curves of UFG alloy. This deformation behavior was absent in the coarse-grained alloy. The Lüdering phenomenon in UFG alloy was attributed to the lack of dislocations in UFG microstructure. A strong dependence of uniform ductility on the average grain size was exhibited by the UFG alloy. Below a critical grain size (0.5 μm), ductility was very limited. Also, with the decrease in grain size, most of the plastic deformation was observed to be localized in necked region of the tensile samples. The negative strain rate sensitivity (SRS) observed for the UFG alloy was opposite of the SRS values reported for UFG alloys in the literature. Based on activation volume measurement, grain boundary mediated dislocation-based plasticity was concluded to be the micro-mechanism operative during plastic deformation of UFG Al–Mg–Sc alloy.

N. Kumar · M. Komarasamy · R. S. Mishra (✉)
Department of Materials Science and Engineering, Center for Friction Stir Processing, University of North Texas, Denton, TX 76203, USA
e-mail: rajiv.mishra@unt.edu

N. Kumar
e-mail: Nilesh.Kumar@unt.edu

M. Komarasamy
e-mail: MageshwariKomarasamy@my.unt.edu

Introduction

Almost two decades of intensive research has gone into understanding the mechanical properties and deformation behavior of ultrafine grained (UFG) materials [1–3]. The scale of UFG microstructure, on the basis of grain size in polycrystalline materials, lies between 1 μm and 100 nm [4]. It is now well established that some of the mechanical properties of UFG materials are superior to, and the deformation behavior is different from their coarse-grained (CG) counterparts (grain size >1 μm) [5]. From mechanical properties point of view, the main motivation to refine grain size comes from the prediction made by Hall–Petch (HP) relationship [6, 7]. HP relationship relates yield strength (YS) and grain size (d) of a polycrystalline material as follows:

$$\sigma_y = \sigma_0 + k_y d^{-1/2} \quad (1)$$

where σ_y, σ_0, and k_y are YS, friction stress, and HP coefficient, respectively. As per this relationship, the YS of a material goes up with a decrease in grain size. For example, the published literature shows that the YS of the CG 5XXX series Al alloys is limited upto 300 MPa. On grain refinement, UFG alloys have shown strength beyond 500 MPa [8–13]. Hence, grain refinement takes the strength level of 5XXX series Al alloys to the category of CG 2XXX and 7XXX Al alloys.

At present, there are various techniques available to obtain UFG microstructure in a wide variety of metals such as Al, Mg, Ti, Fe, etc. and their alloys [5, 14–19]. Among these, severe plastic deformation (SPD) techniques have been widely exploited because of their potential for commercialization in near future. Friction stir processing (FSP) is relatively new among all SPD techniques. Early studies on processing-microstructure-property relationship using FSP were limited to micron-size grain regime. Due to improved understanding of the processing, this technique is now being used to produce UFG microstructure [20–29]. The microstructural evolution during FSP has been studied very extensively. The continued research so far in this area has revealed that the microstructure evolved in the materials processed using FSP is distinctively different from those obtained by other SPD techniques. The grains in the processed region are equiaxed, homogeneous, and have relatively low dislocation density. For example, Su et al. [25] and recently, Ma et al. [26] and Kumar et al. [27–29] reported fraction of high angle grain boundaries (HAGB) to be >90 % in FSP UFG alloys. However, except a few studies concerning microstructure-property relationship in materials processed using FSP, there is a need to explore this relationship further in greater detail.

As mentioned before, UFG materials show very different mechanical properties and unique deformation behaviors. Apart from significant improvement in strength, UFG alloys exhibit enhanced strain rate sensitivity (SRS) [30–33]. Several fold increase in SRS values of UFG FCC materials compared to their CG counterparts have been observed. For example, Wei et al. [31] reported a SRS value of 0.02 for UFG Cu having mean grain size ~200 nm. The SRS of CG Cu is ~0.004 [34]. Hence, UFG Cu showed a five-fold increase in SRS. Although HP relationship has been shown to hold upto a grain size 10 nm in general, Valiev et al. [35] in a recent work have shown that extremely high YS of HPT processed UFG 7475Al and 1570Al cannot be explained on the basis of HP relationship. Another important difference shown by UFG metals and alloys is the presence of tension/compression asymmetry [36]. This has been attributed to an increase in free volume due to higher fraction of grain boundary per unit volume. Yield point phenomenon followed by Lüders band formation is another interesting feature of UFG alloys [37].

Hence, understanding of various properties in UFG regime is important both technologically and scientifically. In spite of such an extensive amount of work on UFG materials, processing of UFG alloy containing equiaxed and dislocation free grains with small distribution in grain size remains a challenge. Moreover, disappointingly low uniform elongation exhibited by UFG remains another handicap for any practical uses of this class of materials. Compilation of the literature data by Koch [38] and Mukai et al. [39] supports this observation.

Although there have been some attempts to understand the underlying deformation mechanisms of UFG alloys, it is still far from fully understood phenomenon. It, therefore, necessitates further research to establish a correlation between microstructure-properties of UFG materials. The present research deals with the plastic deformation behaviors of UFG Al–Mg–Sc alloy. The strength, ductility, SRS, and work hardening rate have been explored for FSP UFG Al–Mg–Sc alloy. Special emphasis has been laid upon the ductility and necking instability. An optical microscope was used to study the neck formation in CG and UFG Al–Mg–Sc alloy. Work hardening rate has been evaluated in terms of grain boundary character and its spacing. Plastic deformation mechanism has been discussed on the basis of SRS measurement experiments.

Experimental details

Processing of the material

A ~3.75-mm-thick twin-roll cast (TRC) Al–Mg–Sc alloy (nominal composition: Al-4Mg-0.8Sc-0.08 wt%Zr) was subjected to various thermo-mechanical processing (TMP) procedures to obtain the alloy in different microstructural conditions. The aging of the alloy was carried out at 563 K (290 °C) for 22 h. FSP was carried out in two different microstructural states: AR and AR+Aged. The FSP of AR and AR+Aged samples were carried out at two different tool rotation rates: 400 and 325 rpm while keeping other FSP parameters same. The details of FSP can be found elsewhere [29]. Table 1 summarizes all the processing conditions under which samples were subjected to quasi-static uniaxial tensile testing.

Uniaxial tensile testing

Samples in various TMP conditions were subjected to uniaxial tensile testing to evaluate the mechanical properties of the alloy. The microstructural state before FSP has an influence on the microstructure evolution during FSP. Different microstructural evolution paths may have its bearing on the mechanical properties. Aging heat treatment at 563 K (290 °C) for 22 h was given to TRC alloy before FSP, and it was followed by tensile testing to study this aspect of processing-property relation. The purpose of testing samples in different TMP conditions was to

Table 1 The thermomechanical conditions of the samples which were subjected to uniaxial tensile testing

Thermomechanical conditions	Uniaxial tensile testing
As-received (AR)	YES
AR+Aged (290 °C, 22 h)	YES
Friction stir processing (FSP)	YES
AR+Aged (290 °C, 22 h)+FSP	YES
AR+Aged (290 °C, 22 h)+FSP+ Aged (290 °C, 22 h)	YES

compare mechanical properties of the samples containing different UFG microstructures. All the testings were carried out at room temperature (RT) at an initial strain rate ($\dot{\varepsilon}$) of 10^{-3} s^{-1}. To determine the SRS value of UFG alloy, the samples were subjected to strain rate jump test. The gage length, width, and thickness of the mini-tensile samples for AR and AR+Aged conditions were 5.00, ~0.95, and 0.95 mm, respectively, and for the rest of the conditions ~5.0, ~1.2, and ~1.0 mm, respectively. All tensile samples were polished using water-based polycrystalline diamond suspension from 15 to 1 μm grit size.

Results and discussion

Quasi-static mechanical properties

Stress–strain and strength–ductility relationships

The engineering stress–engineering strain curves for TRC Al–Mg–Sc alloy in various TMP conditions are shown in Fig. 1. This alloy in AR condition possessed a YS and UTS of 204 ± 4 and 293 ± 4 MPa, respectively. The elongation-to-failure (e_f) is 27.2 ± 1.2 % out of which ~68 % constituted the uniform elongation (e_u). On aging at 563 K (290 °C) for 22 h, the YS increased to 366 ± 8 MPa and UTS to 418 ± 4 MPa. As expected, a significant drop in e_f was observed which changed from 27.2 ± 1.2 % in AR condition to 11.1 ± 3.6 %—a drop of ~60 %. Still, e_u in this condition was ~61 % of e_f. However, after FSP of the alloy in AR condition at 400 rpm (henceforth referred to as UFG-1), not only improvement in the YS and UTS was observed, but e_f was also very high (24.4 %). It should be noted that in spite of a considerable improvement in strength level for UFG-1, the ductility level (e_f) attained

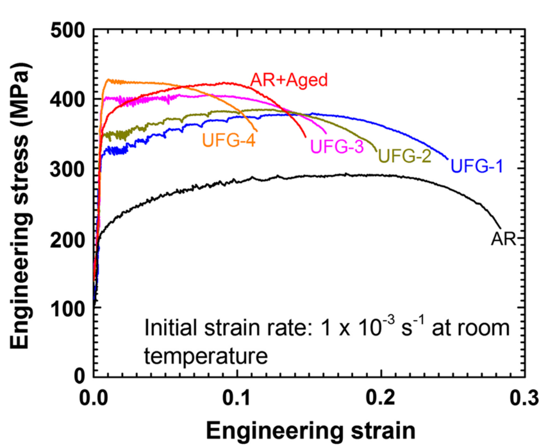

Fig. 1 Engineering stress–engineering strain curves of coarse-grained (CG) and ultrafine-grained (UFG) Al–Mg–Sc alloy (UFG-1: FSP (400 rpm), UFG-2: Aged+FSP (400 rpm), UFG-3: FSP (325 rpm), UFG-4: Aged+FSP (325 rpm))

was quite comparable to that exhibited in AR condition. The YS, UTS, e_f, e_u, and non-uniform elongation e_{nu} for TRC alloy processed under various conditions are summarized in Table 2. As can be noted, the Aged+FSP(325) (henceforth referred to as UFG-4; 325 in the bracket means 325 rpm) showed a strength level better than TRC+Aged condition with almost same level of e_f.

To understand the effect of post-FSP heat treatment, the FSP alloys were subjected to aging heat treatment at 563 K (290 °C) for 22 h. The effects of this aging heat treatment on tensile properties have been shown in the form of histograms in Fig. 2. Aging of UFG-1 showed improvement in YS and UTS, but there was no improvement in YS and UTS on aging of Aged+FSP(400) (henceforth referred to as UFG-2). Unlike UFG-1, FSP(325) (henceforth referred to as UFG-3) did not show any improvement in YS and showed very slight increase in UTS on aging. After aging of UFG-4, like UFG-2, no improvement in YS and UTS was observed. The TRC alloy processed at 400 rpm and 325 rpm with different microstructural conditions responded differently to post-FSP aging heat treatment as far as e_f of the processed alloy is concerned. As can be noted from Fig. 2c, ductility dropped for UFG-1 after aging. This is an expected behavior, because the strength of the TRC alloy in this condition increased after aging. It is well known that the ductility of the alloys decreases as strength increases. Although aging heat treatment did not cause any change in the YS and UTS for UFG-2, a drop in ductility can be observed. In case of aging of UFG-3 and UFG-4 (Aged+FSP(400)+Aged and Aged+FSP(325)+Aged) increase in ductility values are observed. The YS, UTS, and % e_f values of post-FSP samples are summarized in Table 3.

The strength–ductility of the present alloy is shown in Fig. 3 and a comparison has been made with various CG and UFG Al alloys reported in the literature [8–13, 41–45]. Figure 3a shows the variation of YS with e_f of presently investigated TRC CG and UFG Al–Mg–Sc alloy and was compared with 5XXX CG and UFG Al alloys reported in the literature [8–13]. The strength–ductility values for majority of the 5XXX series Al alloys in CG and UFG conditions fall into the band shown in Fig. 3a. However, as can be noted, FSP UFG alloy in some of the TMP conditions lies outside the band. Evidently, FSP resulted in a better combination of strength and ductility. Further comparison of the TRC CG and UFG Al–Mg–Sc alloy with precipitation strengthened 2XXX, 6XXX, and 7XXX Al alloys revealed that strength (YS and UTS) of the presently investigated alloy was better than most of the CG 6XXX Al alloys, and strength was comparable to some of 2XXX and 7XXX Al alloys. For the same strength level, the ductility (e_f) was observed to be better than all these alloys. The variation of YS with ductility for 2XXX, 6XXX, and 7XXX alloys and their comparison with currently investigated alloy are shown

Table 2 The results of uniaxial mini-tensile testing of TRC Al–Mg–Sc alloy in various thermo-mechanical conditions

	YS (MPa)	UTS (MPa)	% e_f	% e_u	% e_{nu}
TRC	204 ± 4	293 ± 4	27.2 ± 1.2	18.6 ± 0.0	8.6 ± 0.9
TRC+Aged	366 ± 8	418 ± 4	11.1 ± 3.6	6.8 ± 2.4	4.3 ± 1.2
FSP(400) (UFG-1)	319 ± 1	384 ± 10	24.4 ± 0.3	14.3 ± 0.2	10.1 ± 0.0
Aged+FSP(400) (UFG-2)	347 ± 1	385 ± 1	20.2 ± 1.4	11.6 ± 0.3	8.6 ± 1.1
FSP(325) (UFG-3)	396 ± 2	405 ± 1	15.2 ± 0.7	7.2 ± 0.6	8.0 ± 0.0
Aged+FSP(325) (UFG-4)	405 ± 19	412 ± 16	11.5 ± 0.9	3.4 ± 1.1	8.1 ± 0.2

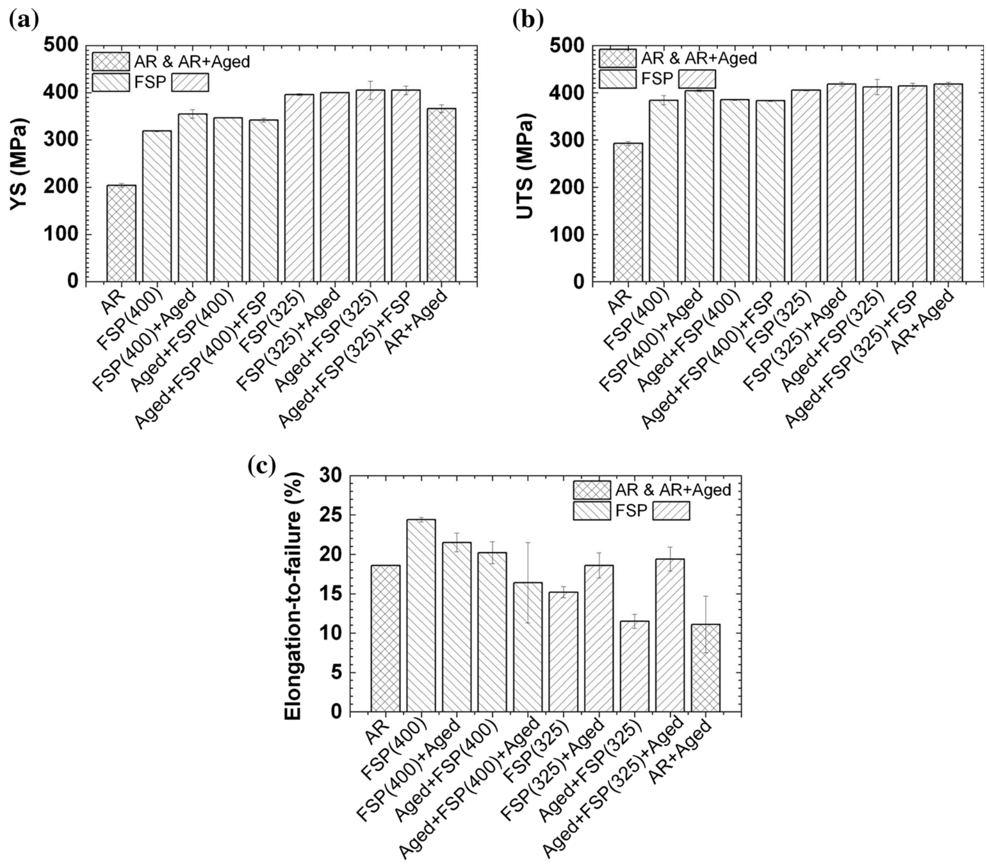

Fig. 2 A comparison of the **a** YS, **b** UTS, and **c** ductility of FSP UFG Al–Mg–Sc alloy with AR and AR+Aged alloy. Included is the effect of pre- and post-FSP aging

in Fig. 3b. The mechanical properties of Al–Mg–Sc with or without Zr have been investigated in the past by many researchers [41–45]. A comparison of the present dataset with those in the literature on Al–Mg–Sc (Zr) showed a superior combination of strength and ductility as illustrated in Fig. 3c.

Ductility of UFG Al–Mg–Sc alloy

Extensive research on UFG alloys has been carried out in last two decades due to their scientific and technological importance [1, 2, 46]. The research carried out so far indicates a significantly different deformation behavior and mechanisms for UFG alloys in comparison with their CG counterparts. A disappointingly low uniform ductility (e_u) shown by UFG alloys has been a bottleneck in the widespread use of these alloys. Compilation of the literature data by Koch [38] and Mukai [39] reveals that elongation (ductility) and grain size are proportionately related, i.e., ductility of the metallic materials decreases with decrease in grain size. To understand the relationship between grain size and ductility of the present UFG alloy, elongation versus grain size plot was created and is shown in Fig. 4a. It shows variation of e_f, e_u, and e_{nu} as a function of average grain size. AR and AR+Aged materials belong to CG regime. As noted by Koch [38] and Mukai [39], here also a wide variation in ductility in these two conditions can be observed. The trend line shown in Fig. 4a does not consider the elongation values of AR+Aged samples. As can be noted, there is a sharp decline in ductility in UFG regime

Table 3 The effect of post-FSP aging heat treatment on the uniaxial tensile mechanical properties of TRC Al–Mg–Sc alloy in various thermo-mechanical conditions

	YS (MPa)	UTS (MPa)	% e_f	% e_u	% e_{nu}
FSP(400)+Aged	355 ± 9	404 ± 2	21.5 ± 1.2	11.1 ± 1.7	10.4 ± 0.5
Aged+FSP(400)+Aged	342 ± 4	383 ± 7	16.4 ± 5.1	9.4 ± 0.4	7.0 ± 5.5
FSP(325)+Aged	400 ± 1	418 ± 4	18.6 ± 1.6	7.3 ± 1.1	11.3 ± 2.6
Aged+FSP(325)+Aged	405 ± 9	414 ± 6	19.4 ± 1.5	4.7 ± 0.0	11.4 ± 1.4

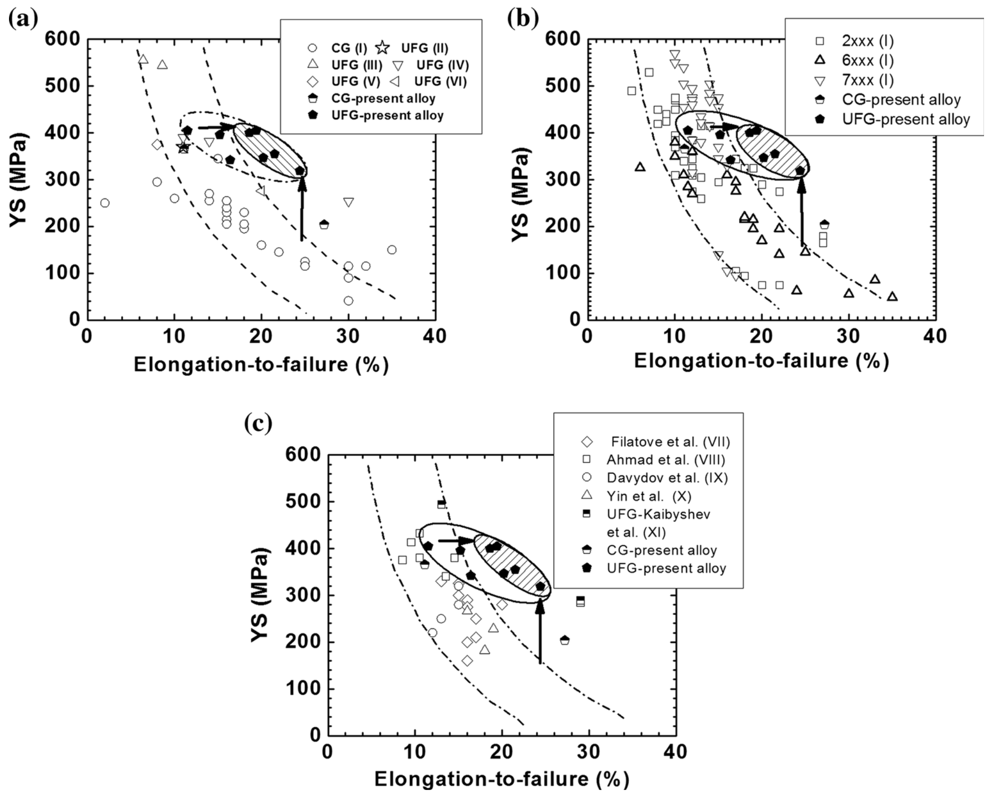

Fig. 3 Comparison of presently investigated Al–Mg–Sc alloys with those in the literature; **a** CG and UFG 5XXX series Al alloys (I–VI: [8–13]), **b** 2XXX, 6XXX, and 7XXX Al alloys (I: [8]), **c** CG and UFG Al–Mg–Sc (Zr) alloys (VII–XI: [41–45])

with decrease in grain size. The UFG-1 (grain size—0.73 ± 0.44 μm) showed a considerably high level of elongation (both in terms of e_f and e_u). Although the total elongation exhibited by UFG-4 (0.39 ± 0.16 μm) was little higher than 10 %, it showed a very small uniform elongation (<4 %). It, therefore, suggests that mere consideration of e_f gives a false impression about the true nature of UFG materials in terms of useful elongation available.

This dependence of uniform ductility on grain size was explained recently by Kumar et al. [27] on the basis of relationship between dislocation mean free path and grain size. It was shown that the dislocation mean free path was of the same order as grain size in UFG-4 material. Direct interaction with HAGB led to enhanced recovery rate. It resulted in lower work hardening capacity of the material and hence early onset of plastic instability. Total elongation, e_f, and uniform elongation, e_u, both showed the same trend with change in grain size. However, with the change in grain size, non-uniform elongation (e_{nu}) part did not change much as evident from the horizontal trend line. It indicates that fraction of e_{nu} increased with the decrease in grain size. The variations in the fraction of e_u and e_{nu} are shown in Fig. 4b. Clearly, the fraction of e_{nu} increased with decrease in grain size, whereas a decrease in the fraction of e_u was observed with decrease in grain size. This increase in non-uniform elongation in UFG samples is reflected in the geometry of the fractured samples in uniaxial tensile testing as well.

UFG and necking phenomenon

In the analysis of work hardening rate of CG material, stress–strain curves upto UTS were considered. In CG material, load drop is generally associated with necking

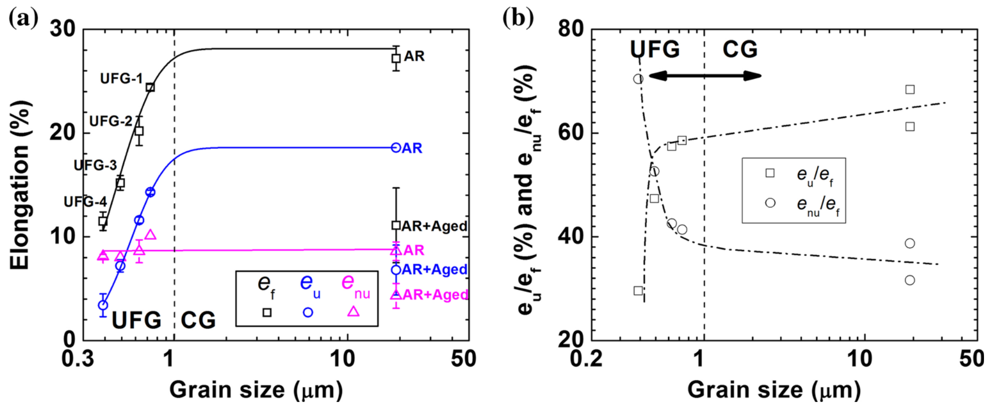

Fig. 4 **a** The variation of elongation as a function of grain size and **b** variation of fraction of uniform and non-uniform elongation as a function of grain size

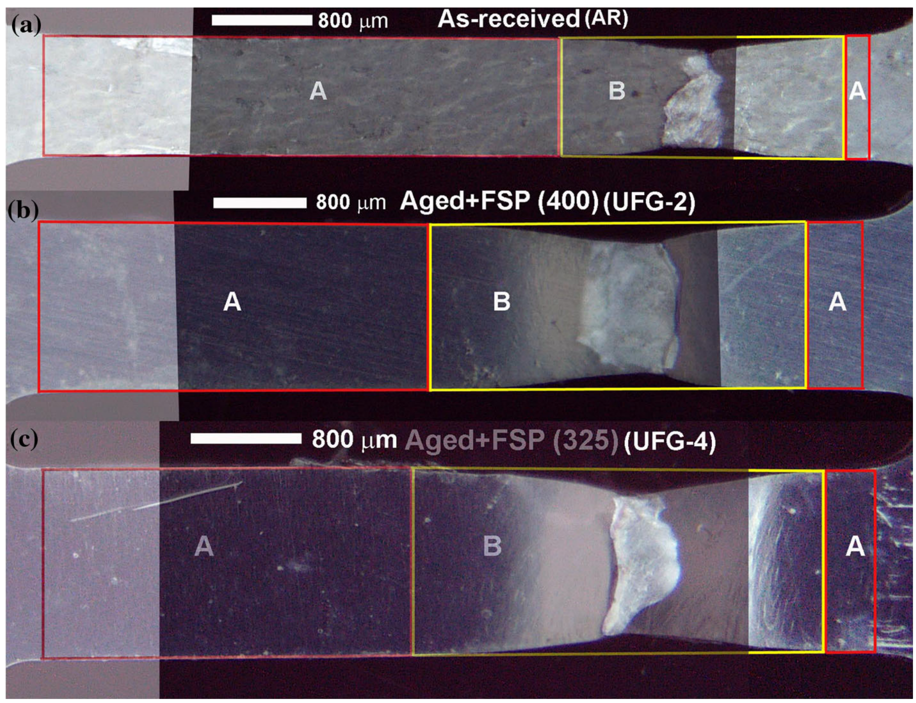

Fig. 5 Mini-tensile fractured sample showing uniformly elongated (**A**) and necked (**B**) regions for **a** AR, **b** UFG-2 and **c** UFG-4 samples

phenomenon when material is tested under uniaxial tensile loading condition. It may not be the case for UFG materials. Fractured mini-tensile samples related to CG and UFG materials in AR, UFG-2, and UFG-4 conditions were observed under optical microscope after uniaxial tensile testing. Both the parts of the fractured mini-tensile samples were joined in image analysis software Adobe Photoshop. These joined samples are shown in Fig. 5. The uniform elongation values were estimated from these fractured samples by measuring the change in width and thickness of regions designated as region A in Fig. 5 (here only top view of the fractured tensile samples is shown). The area marked B represents necked region. The results from this analysis are summarized in Table 4. It should be noted that measured elongation values from fractured samples are close to those obtained from stress–strain curves. The measurement of e_u of UFG-4 was not possible from the optical images due to very small change in dimensions. It can be attributed to the resolution limit of the microscope used and measurement errors.

In recent literature, it has been discussed that necking is delayed in UFG materials due to enhanced SRS [47]. This may be the case where SRS values are very high, such as in the case of superplasticity phenomenon. However, the SRS values lie in the range of 0.01–0.04 for UFG Al alloys [40], and in alloys showing dynamic strain aging (DSA), (as is the case for the presently investigated CG and UFG Al–Mg–Sc alloy) even negative SRS has been reported (see "Strain rate sensitivity and activation volume" Section for a detailed discussion on it). For strain rate sensitive materials, neck instability phenomenon is described using Hart's criterion of neck instability [48]. However, for such

Table 4 Comparison of elongation values measured using LVDT and on fractured samples

	Elongation values measured from fractured samples			Elongation values measured from stress–strain curves		
	e_f	e_u	e_{nu}	e_f	e_u	e_{nu}
AR	24.3 ± 1.0	13.0 ± 3.2	11.4 ± 2.2	27.2 ± 1.2	18.6 ± 0.0	8.6 ± 0.9
UFG-2	17.7 ± 3.3	7.3 ± 1.2	10.4 ± 2.1	20.2 ± 1.4	11.6 ± 0.3	8.6 ± 1.1
UFG-4	12.2 ± 1.2	0.0	12.2 ± 1.2	11.5 ± 0.9	3.4 ± 1.1	8.1 ± 0.2

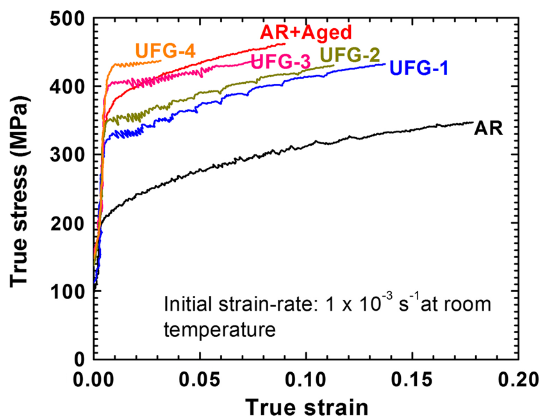

Fig. 6 True stress–strain curves of coarse-grained (CG) and ultrafine-grained (UFG) Al–Mg–Sc alloy (UFG-1: FSP (400 rpm), UFG-2: Aged+FSP (400 rpm), UFG-3: FSP (325 rpm), UFG-4: Aged+FSP (325 rpm))

small values of SRS (either positive or negative), neck formation criterion reduces to the formulation proposed by Considère [49]. Hence, for CG and UFG Al alloys, uniform ductility is mainly governed by strain hardening rate which is greatly influenced by the microstructural state of the material. Kapoor et al. [40] also have pointed out that this level of SRS values of UFG Al alloys might not be sufficient to cause delay in necking in UFG samples tested under tensile conditions. The present result from the measurement of e_u from optical images and from stress–strain curves indicates that necking might have started near UTS in UFG materials also.

Strain hardening rate

As discussed before, strain hardening and uniform ductility exhibited by materials are related. To study the strain hardening behavior of the UFG alloy, engineering stress-engineering strain curves upto UTS were converted into true stress (σ)–true strain (ε) curves (Fig. 6). Specimens AR, AR+Aged, UFG-1, and UFG-2 showed work hardening during deformation. However, UFG-3 exhibited significantly reduced strain hardening capacity, and UFG-4 showed almost a perfectly elasto-plastic behavior. These true stress–strain curves were further used to construct $d\sigma/d\varepsilon$ versus σ plot (Fig. 7). As can be noted, the initial part of the SHR curve corresponding to AR showed a linear decrease in the SHR. The later stage of the work hardening rate curve also showed a linear variation but at a slower rate than the initial stage. This is generally associated with the change in stage III hardening to stage IV hardening [50]. However, it should be emphasized that each stage of work hardening is characterized by characteristic microstructural development, and in the absence of microstructural information, it cannot be confirmed whether such a transition took place during deformation. Like AR material, the alloy in other conditions also showed similar trends in SHR variation. The linear regions of each curve can be approximated with an expression based on Voce law [50] which is given as

$$\frac{d\sigma}{d\varepsilon} = \frac{\alpha G b k_1}{2} - \frac{k_2\sigma}{2} \quad (2)$$

where α, k_1, and k_2 are a constant, a thermal dislocation storage, and recovery terms, respectively. Other symbols have their usual meaning. Linear curve fitting was carried out for upper and lower linear portions of the work hardening rate versus true stress curves and is shown in Fig. 7. In Eq. (2), first term on right-hand side (referred to as θ_o) represents maximum work hardening rate (where macroscopic yielding begins) and second term recovery. In the plot of $d\sigma/d\varepsilon$ versus σ, the slope of the curves represents $k_2/2$. Based on linear curve fitting, θ_o (intercept) and $k_2/2$ (slope) are summarized in Table 5.

The slopes of the lower linear regions of the curves shown in Fig. 7 varied from 3.8 to 15 whereas intercept values from 620 to 1991 (Table 5). From the slope values of lower linear region (which represents rate of recovery) (Table 5), it can be stated that AR+Aged should show minimum uniform elongation whereas maximum value would be expected for UFG-4. However, Table 2 shows that UFG-4 showed minimum uniform elongation. This variation in slopes (3.8–15) can be treated as quite small and concluded that this alloy in different thermo-mechanical conditions exhibits similar rate of recovery in lower linear regime. No clear trend emerges between uniform elongation and intercept values (Table 5) of lower linear regime.

From the intercept values obtained based on the analysis of upper linear region, a clear trend appears to emerge

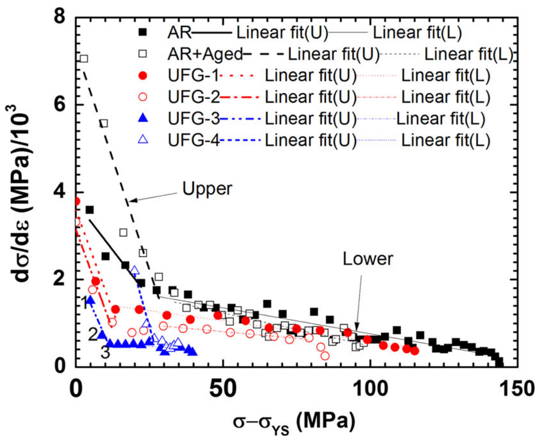

Fig. 7 The Kocks–Mecking (K–M) plot showing work hardening behavior of CG and UFG TRC Al–Mg–Sc alloy

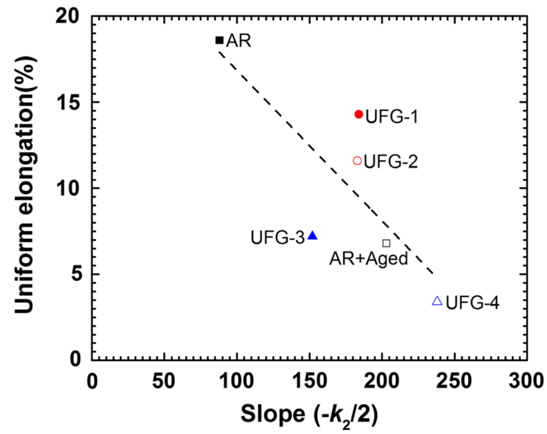

Fig. 8 The variation of uniform elongation as a function of slope of upper linear region of K–M plot in Fig. 7

Table 5 A summary of work hardening parameters obtained by linear curve fitting of work hardening rate curves shown in Fig. 7

Material condition	Upper linear region		Lower linear region	
	Slope ($-k2/2$)	Intercept (θo)	Slope ($-k2/2$)	Intercept (θo)
AR	88	3772	12	1945
AR+Aged	203	7288	15	1991
UFG-1	184	3597	9.3	1520
UFG-2	183	3142	6.2	1118
UFG-3[a]	152 (199)	2210 (2491)	5.2	602
UFG-4	238	6867	3.8	620

([a]Refer to text in "Strain hardening rate" section for the interpretation of values shown in brackets)

between uniform elongation and intercept of this material in different microstructural conditions. However, slope of upper linear region seems to have a better correlation with uniform elongation. The slope of the upper linear region for AR condition was the lowest, whereas the slope was the highest for UFG-4. Figure 8 establishes relationship between uniform elongation and slope of the upper linear region of curves shown in Fig. 7. Overall, uniform ductility appears to follow a linear relationship and decreases with increase in slope or rate of recovery. It should be pointed out here that UFG-3 showed a slope of 152 which was smaller than the slope values of UFG-1 and UFG-2. However, the uniform elongation corresponding to UFG-3 condition was also smaller than that of UFG-1 and UFG-2. It may be a result of insufficient data in the upper linear regime of UFG-3. If for linear curve fitting, only datum points 1 and 2 are considered (Fig. 7), the slope is 199 which is quite close to the slope obtained for AR+Aged (203). The uniform elongation values for UFG-3 and AR+Aged conditions are quite close to each other. Despite such discrepancies, overall, there is a linear relationship between uniform elongation and rate of recovery as evident from Fig. 8.

In UFG materials, higher rate of recovery and hence lower strain hardening rate have been associated with early onset of plastic instability and consequently lower uniform ductility [37, 38, 51, 52]. Since, grain refinement causes flow stress to rise considerably in UFG materials, and at the same time, work hardening rate is impaired due to higher recovery rate; condition of plastic instability [48, 49] during uniaxial tensile testing is met very early resulting in lower uniform elongation. UFG-3 (based on slope calculation using points 1 and 2; Fig. 7) and UFG-4 not only showed a very high rate of recovery compared to others, but also the later part of curve had almost a constant SHR unlike other curves where a gradual decrease in SHR can be observed. It, therefore, appears that high work hardening rate and lower rate of recovery are two very important prerequisites for obtaining an acceptable level of uniform ductility in materials. In fact, Wang et al. [51] successfully induced very high work hardening capability by introducing bimodal grain size distribution using a suitable TMP treatment in nanostructured/UFG copper. The coarser grains in this material provided required work hardening to sustain uniform deformation during the deformation. In the absence of such microstructure, the UFG copper showed almost negligible uniform elongation.

Strain rate sensitivity and activation volume

SRS measurement provides an insight into the deformation mechanisms operative at that length scale. UFG alloys have shown to possess different deformation mechanisms from their CG counterparts. SRS studies on FCC materials have shown that its values increase with decrease in grain size [10, 30, 31, 53, 54]. In the present study, UFG-2 was subjected to strain rate jump test to estimate the SRS of FSP UFG Al–Mg–Sc alloy. It was further used to calculate apparent activation volume. The analytical expression used to calculate SRS is given as

$$m = \frac{\partial \ln \sigma}{\partial \ln \dot{\varepsilon}} \tag{3}$$

where m is SRS. The apparent activation volume, v, is calculated as follows:

$$v = \frac{Mk_{\mathrm{B}}T}{\sigma m} \tag{4}$$

where M, k_{B}, and T are Taylor's factor equal to 3.06 for a polycrystalline FCC material having random texture, Boltzmann constant (J/K), and test temperature (K), respectively.

The result of the strain rate jump test on UFG-2 alloy is shown in Fig. 9a along with the literature data on SRS of FCC and BCC materials as a function of grain size (Fig. 9b). Overall, the trend for FCC materials is an increasing SRS with decreasing grain size. Figure 9a shows the true stress-true strain curves obtained during strain rate jump test. It shows two curves—one was obtained by changing the strain rate from lower (0.001 s^{-1}) to higher (0.01 s^{-1}) and other one from 0.01 to 0.0001 s^{-1}. In each case, the material was deformed at the changed strain rate for a pre-specified amount of strain before changing the strain rate back to the starting value. In the first case, the stress level dropped on raising the strain rate value. In the second case, the stress level increased on decreasing the strain rate from 0.01 to 0.0001 s^{-1}. Also, the changes in stress values are quite different in these two cases. The change in stress value is lower where strain rate was changed from 0.001 to 0.01 s^{-1} compared to the case where strain rate was changed from 0.01 to 0.0001 s^{-1}. It was 10 and 18 MPa, respectively.

The m values calculated using Eq. (3) were quite close, and an average value of −0.011 is shown in Fig. 9b. Clearly, the present alloy showed *negative strain rate sensitivity* (nSRS). In CG Al–Mg alloys, the nSRS phenomenon is quite common [49, 55] and has been associated with DSA phenomenon [49]. Given the fact that FCC UFG Al and its alloys show enhanced SRS (see Fig. 9b for commercially pure Al), nSRS shown by UFG-2 condition is of interest. Careful observation of the stress–strain curves in Fig. 1 reveals that AR alloy shows serrations which are drastically reduced or get eliminated on aging (AR+Aged). However, UFG-1 and UFG-2 both showed pronounced serrations in the stress–strain curves. Hence, nSRS phenomenon observed for UFG Al–Mg–Sc alloy is not unexpected. Also, AR and AR+Aged should show either zero or very small nSRS values. The nSRS in UFG or nanostructured Al alloys has been reported by many other researchers also [56–58]. The nSRS values from the work of these researchers are included in Fig. 9b. Ahn et al. [57] observed a small positive SRS value of 0.0025 for 5083Al alloy having an average grain size of 140 µm which decreased to -0.0108 on refining the grain size to 252 nm. The observation of nSRS was rationalized on the basis of enhanced interaction of solutes and dislocations at grain boundaries by these authors. Solute concentration has been shown to increase with decrease in the grain size [59]. Also, in UFG materials, grain boundaries have been shown to be better source and sink of dislocations [10, 30, 31, 33, 53, 60, 61]. Hence, at lower strain rate, solutes get enough time to pin the dislocations at grain boundaries. It raises the stress level necessary to drive the dislocations and consequently results in nSRS behavior. However, in ECAP processed UFG Al–Mg alloys, nSRS was suppressed. For example, Kapoor et al. [62] reported that Al–Mg alloy exhibited nSRS in

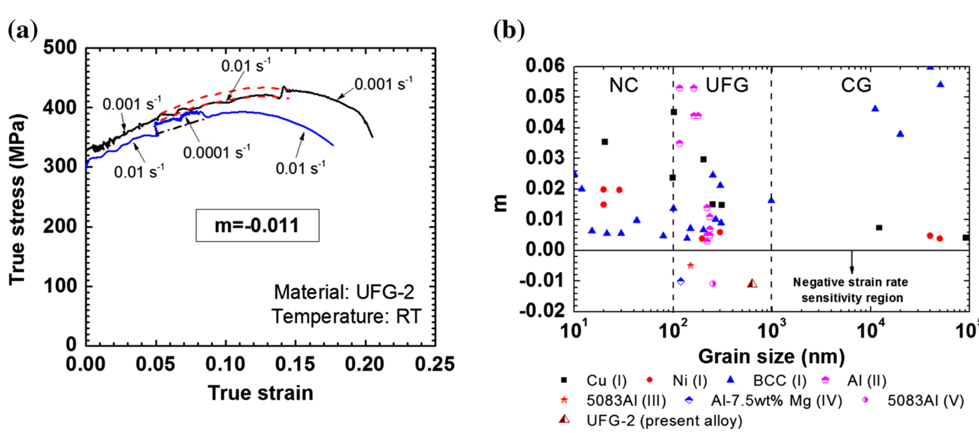

Fig. 9 Plot showing **a** strain rate jump test for UFG-2 alloy for the determination of strain rate sensitivity, and **b** the strain rate sensitivity of several FCC and BCC material along with presently investigated alloy as a function of grain size ranging from CG to NC regime (I–III: [31], IV: [10], V: [56], VI: [58], VII: [57])

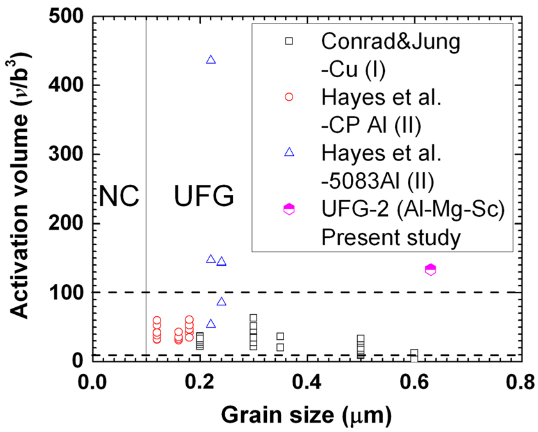

Fig. 10 Activation volume of UFG Al alloys along with the presently investigated FSP UFG alloy as a function of grain size (I, II: [10, 33])

annealed condition, whereas ECAP-12B_C showed a positive SRS. A similar observation was made in an earlier study by Muñoz-Morris et al. [63]. A positive SRS of ECAP processed Al–Mg alloy was rationalized on the basis of high dislocation density in ECAP processed materials causing high number of mobile dislocation and a small number of Mg atoms available per dislocations. It should be noted that FSP is a high temperature processing technique, and microstructure evolved during processing has very low dislocation density. Hence, Mg atoms per dislocation may be sufficient to introduce nSRS in UFG condition.

The apparent activation volume (v) calculated using Eq. (4) is shown in Fig. 10 [10, 33]. In the calculation of v, absolute value of m was used in Eq. (4). For comparison, the literature data on apparent activation volume are shown for UFG FCC materials in the same figure. Evidently, the v value of the UFG-2 alloy is very close to the reported literature data on apparent activation volume for UFG FCC materials. As mentioned before, the knowledge of the activation volume gives an insight into the operative deformation mechanism(s) during plastic deformation of materials. The smallest activation volume is obtained for those processes where vacancy-assisted diffusion processes are operative—for example, Coble creep, grain boundary shear, etc. In such cases, activation volume is expected to be 1–10b^3 [54, 64]. As shown in Fig. 10, in the UFG regime, most of the reported values lie in the range of 10–100b^3 with only a few values lying outside it [33, 53, 65–67]. Wei and Gao [54] have rationalized the activation volume of vacancy-assisted diffusion processes and dislocation-assisted deformation processes as follows:

$$v = \begin{cases} \sim V_a & \text{for vacancy assisted diffusion} \\ \alpha V_a d/b & \text{for dislocation based processes} \end{cases} \quad (5)$$

where V_a and α are atomic volume and a geometrical factor, respectively. For dislocation-based processes, if only atoms associated with dislocation cores are considered, the length of the dislocations which would get activated should be proportional to the grain size. Hence, reduction in grain size would result in a decrease in activation volume. Wei et al. [31] also have considered grain size to be the obstacle spacing in UFG FCC materials in the development of a model to explain the decrease in activation volume with grain size. Conrad and Jung [33] have explained decrease in activation volume by a model based on grain boundary shear promoted by dislocation pile-up models. There may be differences in opinion among researchers about the details of exact mechanism operative during plastic deformation, but the role of grain boundaries as sources and sinks of dislocations has been accepted by many researchers for UFG materials [10, 30, 31, 33, 53, 60, 61]. Based on the activation volume value for UFG-2, it can be speculated that a dislocation-mediated plasticity might be at play, and grain boundaries are probably acting as a source for those dislocations.

Lüders band formation in UFG materials

As mentioned in the Introduction section of this paper, Lüders deformation is another interesting and unique feature of the UFG alloys. The Lüders band formation was observed in currently investigated FSP UFG Al–Mg–Sc alloy. The signature of its formation is embedded in the stress–strain curves in Fig. 1 for UFG-1 to UFG-4 alloys in the form of serrations just after yielding. Such deformation behavior was not exhibited by AR and AR+Aged Al–Mg–Sc alloy. Hence, observation of this phenomenon is not just a manifestation of dislocation-solute interaction, as commonly observed for substitutional and interstitial solid solutions, but also a reflection of complex interplays between dislocations and grain size.

The formation of Lüders deformation bands in fine grained Al and its alloys has been reported by Deep and Plumtree [68], Lloyd and Morris [69], and Wyrzykowski and Grabski [70] in the past and recently by Yu et al. [4], Hung et al. [71], and a few others in UFG Al. Deep and Plumtree [68] attributed occurrence of this phenomenon to the very fine recrystallized microstructure (grain size—0.5 μm to 2 μm) in which all the dislocations were expected to be immobile. Similarly, others also have attributed this deformation behavior to the lack of mobile dislocations [4, 69–71]. To test the hypothesis of lack of mobile dislocations as the origin for the appearance of Lüders deformation in UFG alloys, the present UFG-1 alloy was given 50 % thickness reduction by cold rolling to introduce mobile dislocations in the grain structure. It was followed by mini-tensile testing. In this microstructural condition, no Lüders deformation phenomenon was observed in the stress–strain curve (Fig. 11). Since lack of dislocations is the reason for the occurrence of

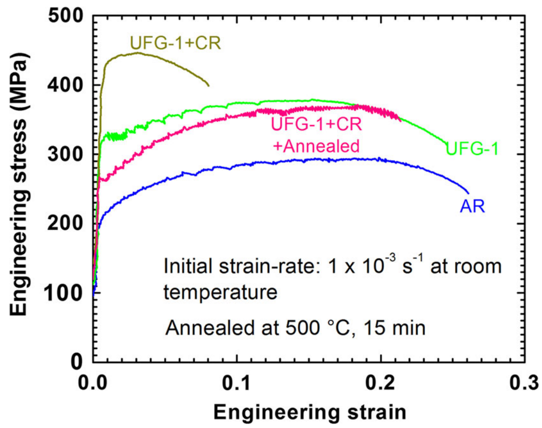

Fig. 11 Stress–strain curves illustrating the microstructural condition necessary for the formation of Lüders bands (UFG-1: AR+FSP (400 rpm))

this phenomenon, the removal of dislocations introduced during rolling should reintroduce the Lüders deformation in the stress–strain curve. The cold-rolled UFG-1 alloy was annealed at 773 K (500 °C) for 15 min and tested. The stress–strain curves indeed showed re-occurrence of this phenomenon (Fig. 11). Hence, annealing at 773 K (500 °C) caused recovery of dislocations thereby making the UFG material mobile dislocation deficient. It, therefore, indicates that the Lüders band formation observed in the present UFG alloy is in fact a result of lack of mobile dislocations.

Conclusions

I. The FSP UFG Al–Mg–Sc alloy showed a discontinuous transition from elastic to plastic regime (Lüders deformation phenomenon). Below a critical grain size (~0.5 µm) stress–strain curve showed elastic-perfectly plastic deformation behavior (UFG-4).

II. Grain size and its distribution play an important role in the determination of the uniform ductility of UFG alloy. UFG-2 having average grain size of 0.63 µm and ~10 % of the grains >1 µm showed a moderately high uniform elongation (11.6 %) whereas UFG-4 having average grain size of 0.39 µm and all the grains <1 µm showed disappointingly very low uniform elongation (3.4 %).

III. The diminishing work hardening capacity of the UFG Al–Mg–Sc alloy can be attributed to reduced intragranular dislocation–dislocation interactions and enhanced dislocation recovery at grain boundaries.

IV. As the average grain size decreases, the majority of the plastic deformation is concentrated in the necked region of the tensile samples.

V. Very high negative strain rate sensitivity observed can be rationalized on the basis of enhanced grain boundary solutes and dislocation interaction at lower strain rate. The corresponding increase in apparent activation volume was similar to the values reported in the literature.

VI. The formation of Lüders band can be attributed to the lack of mobile dislocations in FSP UFG alloy.

Acknowledgements Authors would like to thank The Boeing Company, St. Louis for supplying the material and financial assistance.

References

1. Valiev RZ, Krasilnikov NA, Tsenev NK (1991) Plastic deformation of alloys with submicron-grained structure. Mater Sci Eng, A 137:35–40
2. Gleiter H (1992) Materials with ultrafine microstructures: retrospectives and perspectives. Nanostruct Mater 1:1–19
3. Valiev RZ, Kozlov EV, Ivanov YF, Lian J, Nazarov AA, Baudelet B (1994) Deformation behaviour of ultra-fine-grained copper. Acta Metall Mater 42:2467–2474
4. Yu CY, Kao PW, Chang CP (2005) Transition of tensile deformation behaviors in ultrafine-grained aluminum. Acta Mater 53:4019–4028
5. Valiev RZ, Islamgaliev RK, Alexandrov IV (2000) Bulk nanostructured materials from severe plastic deformation. Prog Mater Sci 45:103–189
6. Hall EO (1951) The deformation and ageing of mild steel: III discussion of results. Proc Phys Soc B 64:747–753
7. Petch NJ (1953) The cleavage strength of polycrystals. Iron Steel Inst 174:25–28
8. Kaufman JG (1999) Properties of aluminum alloys: tensile, creep, and fatigue data at high and low temperatures. ASM International, Materials Park
9. Tellkamp VL, Melmed A, Lavernia EJ (2001) Mechanical behavior and microstructure of a thermally stable bulk nanostructured Al alloy. Metall Mater Trans A 32:2335–2343
10. Hayes RW, Witkin D, Zhou F, Lavernia EJ (2004) Deformation and activation volumes of cryomilled ultrafine-grained aluminum. Acta Mater 52:4259–4271
11. Higashi K, Patlan V, Kitagawa K, Kawazoe M (2001) Tensile and low-cycle fatigue properties of heat treated ultra-fine grain 5056 aluminum alloy. J Japan Inst Light Met 51:646–650
12. Stolyarov VV, Lapovok R (2004) Effect of backpressure on structure and properties of AA5083 alloy processed by ECAP. J Alloys Compd 378:233–236
13. Chang SY, Lee JG, Park KT, Shin DH (2001) Microstructures and mechanical properties of equal channel angular pressed 5083 Al alloy. Mater Trans 42:1074–1080
14. Valiev RZ, Langdon TG (2006) Principles of equal-channel angular pressing as a processing tool for grain refinement. Prog Mater Sci 51:881–981
15. Zhilyaev AP, Langdon TG (2008) Using high-pressure torsion for metal processing: fundamentals and applications. Prog Mater Sci 53:893–979
16. Saito Y, Utsunomiya H, Tsuji N, Sakai T (1999) Novel ultra-high straining process for bulk materials—development of the accumulative roll-bonding (ARB) process. Acta Mater 47:579–583

17. Tsuji N, Saito Y, Lee S-H, Minamino Y (2003) ARB (Accumulative Roll-Bonding) and other new techniques to produce bulk ultrafine grained materials. Adv Eng Mater 5:338–344
18. Mishra RS, Ma ZY (2005) Friction stir welding and processing. Mater Sci Eng, R 50:1–78
19. Witkin DB, Lavernia EJ (2006) Synthesis and mechanical behavior of nanostructured materials via cryomilling. Prog Mater Sci 51:1–60
20. Kwon YJ, Saito N, Shigematsu I (2002) Friction stir process as a new manufacturing technique of ultrafine grained aluminum alloy. J Mater Sci Lett 21:1473–1476
21. Su J-Q, Nelson TW, Sterling CJ (2003) A new route to bulk nanocrystalline materials. J Mater Res 18:1757–1760
22. Charit I, Mishra RS (2005) Low temperature superplasticity in a friction-stir-processed ultrafine grained Al–Zn–Mg–Sc alloy. Acta Mater 53:4211–4223
23. Ma ZY, Mishra RS (2005) Development of ultrafine-grained microstructure and low temperature (0.48 T_m) superplasticity in friction stir processed Al–Mg–Zr. Scripta Mater 53:75–80
24. Argade GR, Yuan W, Kandasamy K, Mishra RS (2012) Stress corrosion cracking susceptibility of ultrafine grained AZ31. J Mater Sci 47:6812. doi:10.1007/s10853-012-6625-6
25. Su JQ, Nelson TW, Sterling CJ (2006) Grain refinement of aluminum alloys by friction stir processing. Philos Mag 86:1–24
26. Ma ZY, Liu FC, Mishra RS (2010) Superplastic deformation mechanism of an ultrafine-grained aluminum alloy produced by friction stir processing. Acta Mater 58:4693–4704
27. Kumar N, Mishra RS, Huskamp CS, Sankaran KK (2011) Critical grain size for change in deformation behavior in ultrafine grained Al–Mg–Sc alloy. Scripta Mater 64:576–579
28. Kumar N, Mishra RS, Huskamp CS, Sankaran KK (2011) Microstructure and mechanical behavior of friction stir processed ultrafine grained Al–Mg–Sc alloy. Mater Sci Eng, A 528:5883–5887
29. Kumar N, Mishra RS (2013) Ultrafine-grained Al–Mg–Sc alloy via friction-stir processing. Metall Mat Trans A 44:934–945
30. May J, Höppel HW, Göken M (2005) Strain rate sensitivity of ultrafine-grained aluminium processed by severe plastic deformation. Scripta Mater 53:189–194
31. Wei Q, Cheng S, Ramesh KT, Ma E (2004) Effect of nanocrystalline and ultrafine grain sizes on the strain rate sensitivity and activation volume: fcc versus bcc metals. Mater Sci Eng, A 381:71–79
32. Ding Y, Jiang J, Shan A (2009) Plastic instability and strain rate sensitivity of ultrafine-grained iron. J Alloys Compd 487:517–521
33. Conrad H, Jung K (2005) On the strain rate sensitivity of the flow stress of ultrafine-grained Cu processed by equal channel angular extrusion (ECAE). Scripta Mater 53:581–584
34. Carreker RP Jr, Hibbard WR Jr (1953) Tensile deformation of high-purity copper as a function of temperature, strain rate, and grain size. Acta Metall 1:654–663
35. Valiev RZ, Enikeev NA, Murashkin MY, Kazykhanov VU, Sauvage X (2010) On the origin of the extremely high strength of ultrafine-grained Al alloys produced by severe plastic deformation. Scripta Mater 63:949–952
36. Yapici GG, Beyerlein IJ, Karaman I, Tomé CN (2007) Tension–compression asymmetry in severely deformed pure copper. Acta Mater 55:4603–4613
37. Tsuji N, Ito Y, Saito Y, Minamino Y (2002) Strength and ductility of ultrafine grained aluminum and iron produced by ARB and annealing. Scripta Mater 47:893–899
38. Koch CC (2003) Ductility in nanostructured and ultra fine-grained materials: recent evidence for optimism. J Meta Nanocryst Mater 18:9–20
39. Mukai T, Kawazoe M, Higashi K (1998) Dynamic mechanical properties of a near-nano aluminum alloy processed by equal-channel-angular-extrusion. Nanostruct Mater 10:755–765
40. Kapoor R, De PS, Mishra RS (2010) An analysis of strength and ductility of ultrafine grained Al alloys, Mate. Sci Forum 633–634:165–167
41. Filatov YA, Yelagin VI, Zakharov VV (2000) New Al–Mg–Sc alloys. Mater Sci Eng, A 280:97–101
42. Ahmad Z (2003) The properties and application of scandium-reinforced aluminum. JOM 55(3):35–39
43. Davydov VG, Elagin VI, Zakharov VV, Rostova TD (1996) Alloying aluminum alloys with scandium and zirconium additives. Met Sci Heat Treat 38:347–352
44. Yin Z, Pan Q, Zhang Y, Jiang F (2000) Effect of minor Sc and Zr on the microstructure and mechanical properties of Al–Mg based alloys. Mater Sci Eng A 280:151–155
45. Kaibyshev R, Sitdikov O, Olenyov S (2002) Ultrafine grain formation during equal channel angular extrusion in an Al–Mg–Sc Alloy. In: Zhu YT, Langdon TG, Mishra RS, Semiatin SL, Saran MJ, Lowe TC (eds) Ultrafine grained materials II. TMS Annual Meeting, Seattle, pp 65–74
46. Valiev RZ, Vishnyakov YD, Mulyukov RR, Fainshtein GS (1990) On the decrease of curie temperature in submicron-grained nickel. Phys Status Solidi A 117:549–553
47. Sabirov I, Estrin Y, Barnett MR, Timokhina I, Hodgson PD (2008) Enhanced tensile ductility of an ultra-fine-grained aluminum alloy. Scripta Mater 58:163–166
48. Hart EW (1967) Theory of the tensile test. Acta Metall 15:351–355
49. Dieter GE (1988) Mechanical metallurgy. McGraw-Hill, Singapore
50. Kocks UF, Mecking H (2003) Physics and phenomenology of strain hardening: the FCC case. Prog Mater Sci 48:171–273
51. Wang Y, Chen M, Zhou F, Ma E (2002) High tensile ductility in a nanostructured metal. Nature 419:912–915
52. Ma E (2003) Instabilities and ductility of nanocrystalline and ultrafine-grained metals. Scripta Mater 49:663–668
53. Torre D, Pereloma EV, Davies CHJ (2004) Strain rate sensitivity and apparent activation volume measurements on equal channel angular extruded Cu processed by one to twelve passes. Scripta Mater 51:367–371
54. Wei Y, Gao H (2008) An elastic–viscoplastic model of deformation in nanocrystalline metals based on coupled mechanisms in grain boundaries and grain interiors. Mater Sci Eng, A 478:16–25
55. Kubin LP, Chihab K, Estrin Y (1988) The rate dependence of the portevin-Le chatelier effect. Acta Metall 36:2707–2718
56. Han BQ, Huang J, Zhu YT, Lavernia EJ (2006) Negative strain-rate sensitivity in a nanostructured aluminum alloy. Adv Eng Mater 8:945–947
57. Ahn B, Mitra R, Lavernia EJ, Nutt SR (2010) Effect of grain size on strain rate sensitivity of cryomilled Al–Mg alloy. J Mater Sci 45:4790. doi:10.1007/s10853-010-4664-4
58. Fan GJ, Wang GY, Choo H, Liaw PK, Park YS, Han BQ, Lavernia EJ (2005) Deformation behavior of an ultrafine-grained Al–Mg alloy at different strain rates. Scripta Mater 52:929–933
59. Sha G, Yao L, Liao X, Ringer SP, Duan ZC, Langdon TG (2011) Segregation of solute elements at grain boundaries in an ultrafine grained Al–Zn–Mg–Cu alloy. Ultramicroscopy 111:500–505
60. Meyers MA, Mishra A, Benson DJ (2006) Mechanical properties of nanocrystalline materials. Prog Mater Sci 51:427–556
61. Blum W, Zeng XH (2009) A simple dislocation model of deformation resistance of ultrafine-grained materials explaining Hall–Petch strengthening and enhanced strain rate sensitivity. Acta Mater 57:1966–1974
62. Kapoor R, Gupta C, Sharma G, Chakravartty JK (2005) Deformation behavior of Al–1.5 Mg processed using the equal channel angular pressing technique. Scripta Mater 53:1389–1393
63. Muñoz-Morris MA, Garcia OC, Morris DG (2003) Mechanical behaviour of dilute Al–Mg alloy processed by equal channel angular pressing. Scripta Mater 48:213–218

64. Conrad H, Narayan J (2002) Mechanisms for grain size hardening and softening in Zn. Acta Mater 50:5067–5078
65. Wang YM, Ma E (2004) Three strategies to achieve uniform tensile deformation in a nanostructured metal. Acta Mater 52:1699–1709
66. Li YJ, Zeng XH, Blum W (2004) Transition from strengthening to softening by grain boundaries in ultrafine-grained Cu. Acta Mater 52:5009–5018
67. Conrad H, Yang D (2002) Plastic deformation kinetics of electrodeposited Cu foil at low and intermediate homologous temperatures. J Electron Mater 31:304–312
68. Deep G, Plumtree A (1975) Yield point behavior in extruded aluminum rod. Metall Trans A6:359–366
69. Lloyd DJ, Morris LR (1977) Luders band deformation in a fine grained aluminium alloy. Acta Metall 25:857–861
70. Wyrzykowski JW, Grabski MW (1982) Lüders deformation in ultrafine-grained pure aluminium. Mater Sci Eng 56:197–200
71. Hung PC, Sun PL, Yu CY, Kao PW, Chang CP (2005) Inhomogeneous tensile deformation in ultrafine-grained aluminum. Scripta Mater 53:647–652